Ceramics International 48 (2022) 13163–13174

Contents lists available at ScienceDirect

Ceramics International

journal homepage: www.elsevier.com/locate/ceramint

Parallel-solution blow spun Al-SnO_2/F-SnO_2 fibers as an efficient room temperature ethanol sensor

Emanuel P. Nascimento [a,b,*], Rondinele N. Araujo [a,b], Hellen C.T. Firmino [a,b], Valmor R. Mastelaro [c], Francisco J.A. Loureiro [d], Gelmires A. Neves [b], Eliton S. Medeiros [e], Romualdo R. Menezes [b,**]

[a] Graduate Program in Materials Science and Engineering, Federal University of Campina Grande, Campina Grande, PB, Brazil
[b] Laboratory of Materials Technology (LTM), Department of Materials Engineering, Federal University of Campina Grande, Campina Grande, PB, Brazil
[c] Laboratory of Nanomaterials and Advanced Ceramics (NACA), São Carlos Institute of Physics, USP, São Carlos, SP, Brazil
[d] Centre of Mechanical Technology and Automation (TEMA), Department of Mechanical Engineering, University of Aveiro, 3810-193, Aveiro, Portugal
[e] Materials and Biosystems Laboratory, Federal University of Paraíba, Cidade Universitária, João Pessoa, PB, Brazil

ARTICLE INFO

Keywords:
F-doped SnO_2 fibers
Al-doped SnO_2 fibers
Solution blow spinning
Parallel-spinning
Ethanol sensor

ABSTRACT

In the last few years, the design of room-temperature gas sensors is in growing demand. This is because high operating temperatures increase power consumption and impose unnecessary risks when working with flammable gases. This article describes the parallel-spinning fabrication of Al–SnO_2/F–SnO_2 hybrid fibers using the Solution Blow Spinning (SBS) method for room-temperature ethanol sensing application. The structural influence of element doping and the chemical composition/elemental states were studied by X-ray diffraction (XRD), Raman spectroscopy and X-ray photoelectron spectroscopy (XPS). The 5 at% Al–SnO_2/15 at% F–SnO_2 composite-based sensor exhibited high sensitivity to ethanol ($R = 3.0$ at 100 ppm) at room temperature. This sensor also showed short response/recovery times, excellent selectivity, repeatability and long-term stability. More importantly, the sensor based on Al–SnO_2/F–SnO_2 composite displayed a sensing response 9 times higher than pure SnO_2 fibers. These results indicate that the Al–SnO_2/F–SnO_2 fibers prepared in this work are promising and excellent room temperature sensing materials.

1. Introduction

The fabrication of reliable, robust and portable gas sensors that work at low temperatures is a topic of great research interest, mainly driven by the need for low-cost devices. Many materials offer high sensing performance at low temperatures, such as semiconducting polymers (e.g., polyaniline and polypyrrole), ferrites, high-surface-area nanomaterials and metal oxide semiconductors (MOS). Tin dioxide (SnO_2) is well known as one of the most efficient gas sensing materials due to its sensitivity to many oxidizing [1–3] and reducing [4–7] gases. Generally, pure SnO_2 alone does not present high sensitivity, fast response and good selectivity to any gas at room temperature, requiring higher temperatures (200–400 °C) to display optimal sensing performance [7–9]. The high temperatures increase energy consumption and are hazardous to human life, particularly under inflammable gas environments [10]. Under these circumstances, it is essential to develop safe and robust sensors capable of showing good sensitivity, selectivity, long-term stability and fast response/recovery rates at low working temperatures.

Oxygen vacancy engineering [2,11], fabrication of 1D, 2D and 3D nanomaterials [12], doping [5,10], noble metal loading [13,14] and composite/hybrid materials [6,15] are among the various strategies to promote the sensing performance of SnO_2. Often, the appropriate strategy must consider at least one of the following reasons: (i) increase in surface area and active sites on the surface; (ii) increase in the number of oxygen vacancies and other defects; (iii) chemical sensitization of the surface, contributing to increasing oxygen adsorption; and (iv) formation of p-n heterojunctions between composite nanomaterials. The development of micro and nanofibers of SnO_2-based composites is an

* Corresponding author. Laboratory of Materials Technology (LTM), Department of Materials Engineering, Federal University of Campina Grande (UFCG), Av. Aprígio Veloso 882, Campina Grande, PB, 58429-900, Brazil.
** Corresponding author. Laboratory of Materials Technology (LTM), Department of Materials Engineering, Federal University of Campina Grande (UFCG), Av. Aprígio Veloso 882, Campina Grande, PB, 58429-900, Brazil.
E-mail addresses: emanuel.nascimento@ufcg.edu.br (E.P. Nascimento), romualdo.menezes@ufcg.edu.br (R.R. Menezes).

https://doi.org/10.1016/j.ceramint.2022.01.193
Received 12 July 2021; Received in revised form 17 January 2022; Accepted 18 January 2022
Available online 22 January 2022

interesting strategy to obtain improved gas sensors due to the easy preparation, cost-effectiveness, and creation of structural and electronic defects within the matrix. Besides, one-dimensional (1D) SnO_2 nanomaterials have a high surface-to-volume ratio [15] and directional morphology that facilitates electron transport and interaction with target gas molecules [16]. These characteristics provide enhanced sensing results at low working temperatures and, therefore, are ideal for commercial applications. For instance, Wang, et al. [15] produced $NiCo_2O_4$@SnO_2 heterostructure nanofibers via a combination of electrospinning and hydrothermal methods. The composite-based sensor exhibited high sensitivity to ethanol (8.87 at 100 ppm) at a temperature of 160 °C. Hsu et al. [3] reported the preparation of Au-functionalized SnO_2/In_2O_3 nanofibers by a simple electrospinning method and gold sputtering. They achieved good CO gas sensitivities at temperatures as low as 150 °C. Bai et al. [17] developed room-temperature NO_2 sensors with a low detection limit (10 ppb) and fast response/recovery times (2.2 and 10.5 s, respectively) by growing thin-layered MoS_2 nanoflakes on SnO_2 nanotubes. Bang et al. [1] reported the synthesis of SnS/SnO_2 nanowires with efficient NO_2 gas sensing at a low temperature (100 °C). On the other hand, electrospinning is the main method for the preparation of heterogeneous 1D nanostructures [18]. However, it possesses some limitations regarding the low productivity rate and the limited range of solvents for solution preparation. The solution blow spinning (SBS) technique is an alternative for preparing ceramic micro and nanofibers with high productivity rates, low operating costs and solvent flexibility [10,19–22]. The flexibility of electrospinning allows the development of new ways to produce composite fibers, such as co-electrospinning [23,24] and parallel electrospinning [25]. However, since the development of SBS in 2009 [26], similar spinning setups have not been explored to produce highly functional composite nanomaterials. Furthermore, to our knowledge, no work has reported the synthesis of F–SnO_2/Al–SnO_2 by separately doping SnO_2 to generate a hybrid-like material for gas sensing applications. Therefore, in this work, we report for the first time the parallel-spinning of F-doped SnO_2/Al-doped SnO_2 fibers by SBS as a novel material for a room temperature ethanol sensor with reproducible and stable sensing properties. The morphological, structural and electrical properties of the Al–SnO_2/F–SnO_2 fibers were also systematically investigated. A mechanism was proposed to explain the improved ethanol detection performance of the Al–SnO_2/F–SnO_2 fibers.

2. Materials and methods

2.1. Materials

Tin (II) chloride dihydrate ($SnCl_2{\cdot}2H_2O$, ≥98.0%, Sigma-Aldrich, Brazil), ammonium fluoride (NH_4F, ≥98.0%, Sigma-Aldrich, Brazil) and aluminum nitrate nonahydrate ($(Al(NO_3){\cdot}9H_2O$, ≥98%, Neon, Brazil) were used as ceramic precursors. Poly (vinyl acetate) (PVAc, Mw = ~500,000 g mol^{-1}, Sigma-Aldrich, Brazil) was used as spinning aid. Acetic acid (99,7%, Dinâmica, Brazil) and ethanol (99.5%, Synth, Brazil) were used as solvents.

2.2. Fabrication of Al–SnO_2/F–SnO_2 fibers

The Al–SnO_2/F–SnO_2 fibers were fabricated by simultaneously spinning (parallel-spinning) two separate solutions (Fig. 1). The first solution was prepared as follows: 1 g of tin (II) chloride dihydrate was added to a 4:1 (v/v) acetic acid/ethanol solution and stirred for 1 h. After that, 15 at% NH_4F was added to this solution and vigorously stirred for 1 h. Subsequently, 10 w/v% poly (vinyl acetate) was added and mixed at 60 °C for 1 h to form a clear solution. The second solution was prepared similarly by modifying the type and content of the dopant added. For this solution, $Al(NO_3){\cdot}9H_2O$ was added to produce the Al-doped SnO_2 fibers with 1, 3 and 5 at% Al. For comparison, SnO_2 (without any dopants) and 15 at% F-doped SnO_2 (15FTO) were prepared under similar conditions. The final compositions were designated as SnO_2, 15FTO, 1Al/15FTO, 3Al/15FTO and 5Al/15FTO. In this work, we prepared SnO_2 nanofibers doped with 15 at% F based on a previously published work that demonstrated this percentage to be ideal for ethanol gas sensing at RT [10].

Hybrid fibers were spun immediately after precursor solution preparation using the spinning apparatus described in Fig. 1. The SBS parallel spinning system consists of two injection pumps, wherein the plastic syringes with the precursor solutions are placed and connected to spinning nozzles. A heated collector helped dry the fibers as they were spun. The solutions were force-fed at a feeding rate of 6 mL/h through an inner-nozzle with an internal diameter of 0.7 mm. A constant air pressure (0.34 MPa) was blown through the outer nozzle as the driving force for fiber spinning. The spinning parameters were kept constant during the preparation of all compositions. The as-spun fibers were subjected to calcination under atmospheric air for 3 h in a muffle furnace at 600 °C and 5 °C.min^{-1} heating rate to remove the polymer and induce the formation of the Al and F-doped SnO_2 fibers.

2.3. Characterization

Fiber morphology was characterized by scanning electron microscopy (SEM) (TESCAN, VEGA 3). Fiber diameters were measured for ~100 fibers using the Image J software (National Institutes of Health, USA). X-ray diffraction (XRD) was performed (Shimadzu, XRD-6000) using CuKα X-ray source (1.5418 Å). Raman spectroscopy was carried

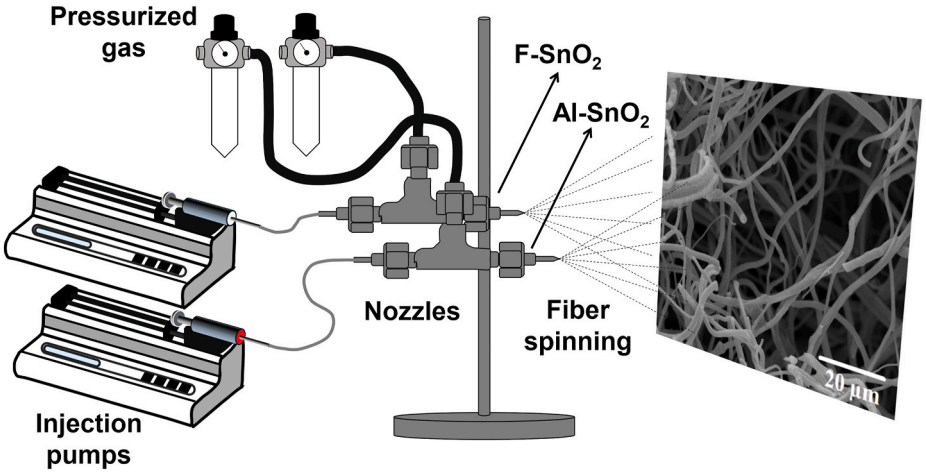

Fig. 1. The gas sensing mechanism of Al–SnO_2/F–SnO_2 fibers exposed to ethanol gas.

out by a Renishaw inVia Raman spectrometer with an excitation laser wavelength of 532 nm (laser power of 5% and 3 accumulations). X-ray photoelectron spectra (XPS) were recorded using a Scienta Omicron ESCA + spectrometer with a high-performance hemispheric analyzer (EAC2000) and monochromatic Al Kα radiation of 1486.6 eV. The XPS data were analyzed using the CASA XPS software. N_2 adsorption/desorption isotherm was determined by volumetric method using a Micromeritics TriStar 3000 instrument. The specific surface area was calculated using the Brunauer-Emmett-Teller (BET) isotherm model. Current-voltage (I–V) characteristics were obtained using a Nanovoltmeter Keithley 2182A.

2.4. Ethanol gas-sensing performance

The sensors were fabricated by ultrasonically dispersing the calcined fibers in isopropyl alcohol and depositing them onto a glass substrate (4 cm^2 glass slides) with a pair of copper wires, following a procedure described in previous work [10]. The mass of fibers deposited for each sensor was 25 mg. Two Cu wires were attached to the glass substrates using epoxy resin (Fig. 2A) to prepare the electrodes. The gas-sensing tests were performed in homemade testing equipment composed of a glass chamber and a nanovoltmeter Keithley 2182A connected to a computer (Fig. 2B). The static liquid-gas distribution method was used to obtain the desired ethanol concentration [27], which was injected into the testing chamber and mixed with air. The volume of ethanol injected to achieve the desired concentration was determined by the formula [27,28]:

$$V_1 = \frac{C \times M \times V_2}{22.4 \times \rho \times \varphi \times 1000} \quad (1)$$

where C (ppm) is the target gas concentration, ρ (g/mL) is the density of the liquid, φ is the required gas volume fraction, V_1 (μL) is the volume of the liquid, V_2 (L) is the volume of the glass chamber, and M (g/mol) is the molecular weight of the liquid. For the measurements, the power supply was attached to the copper wires, and a constant current of 80 nA was applied throughout the tests, while a nanovoltmeter Keithley 2182A recorded the data in real-time. When the voltage of each sensor reached a steady state for each gas concentration, the chamber was opened to recover the sensor in air ambient. The voltage values were converted into resistance values. The sensing response (R) is defined as $R = (R_{air}/R_{gas})/R_{air}$, where R_{air} is the sensor resistance in atmospheric air and R_{gas} is the resistance in a constant concentration of ethanol [28].

3. Results and discussion

3.1. Morphological and structural analyses of $Al/SnO_2/F–SnO_2$ sensors

Scanning electron microscopy was performed on the samples to study fiber morphology before and after calcination. SEM micrographs presented in Fig. 3A and D shows that the as-spun fibers consist of continuous structures with a round cross-section and smooth surface. The fibers presented a diameter distribution and mean diameters ranging from 1625 ± 749 nm to 2496 ± 827 nm. The large fiber diameter may have resulted from polymer chain relaxation after high-pressure spinning. The relaxation caused the fibers to shrink, resulting in a consequent increase in fiber diameter to maintain a constant volume of material. PVAc is known to have a glass transition temperature (T_g) between 28 and 35 °C [29]. The fibers were collected in a heated collector (T~50 °C) to facilitate solvent evaporation. This temperature above T_g allowed polymer chains to move freely, causing chain relaxation and fiber shrinkage. The SEM images of fibers calcined at 600 °C (Fig. 3B and E) displayed a continuous morphology with rough surfaces. The calcination eliminated the organic material, forming the ceramic fibers and reducing fiber diameter. The calcined pure SnO_2 and Al/FTO fibers exhibited mean diameters that ranged from 718 ± 229 nm to 1506 ± 498 nm and reached several microns in length. The samples presented continuous fiber morphology with intimate contact between fibers. This intertwined fiber structure plays a key role in electron transport [30] and, thereby, is beneficial for solid-state gas sensors. Fig. 3C and F shows X-ray fluorescence mapping of the 1Al/15FTO and

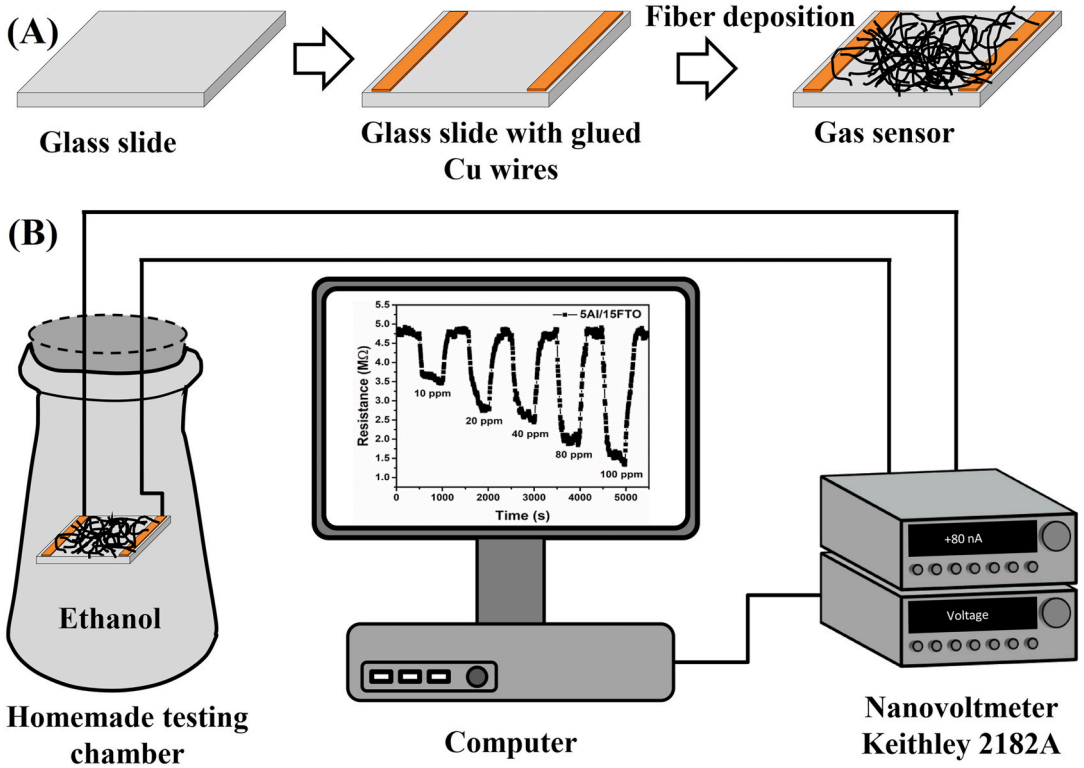

Fig. 2. (A) Schematic illustration of sensor fabrication with Cu wires. (B) Schematic diagram of the ethanol gas sensing test system.

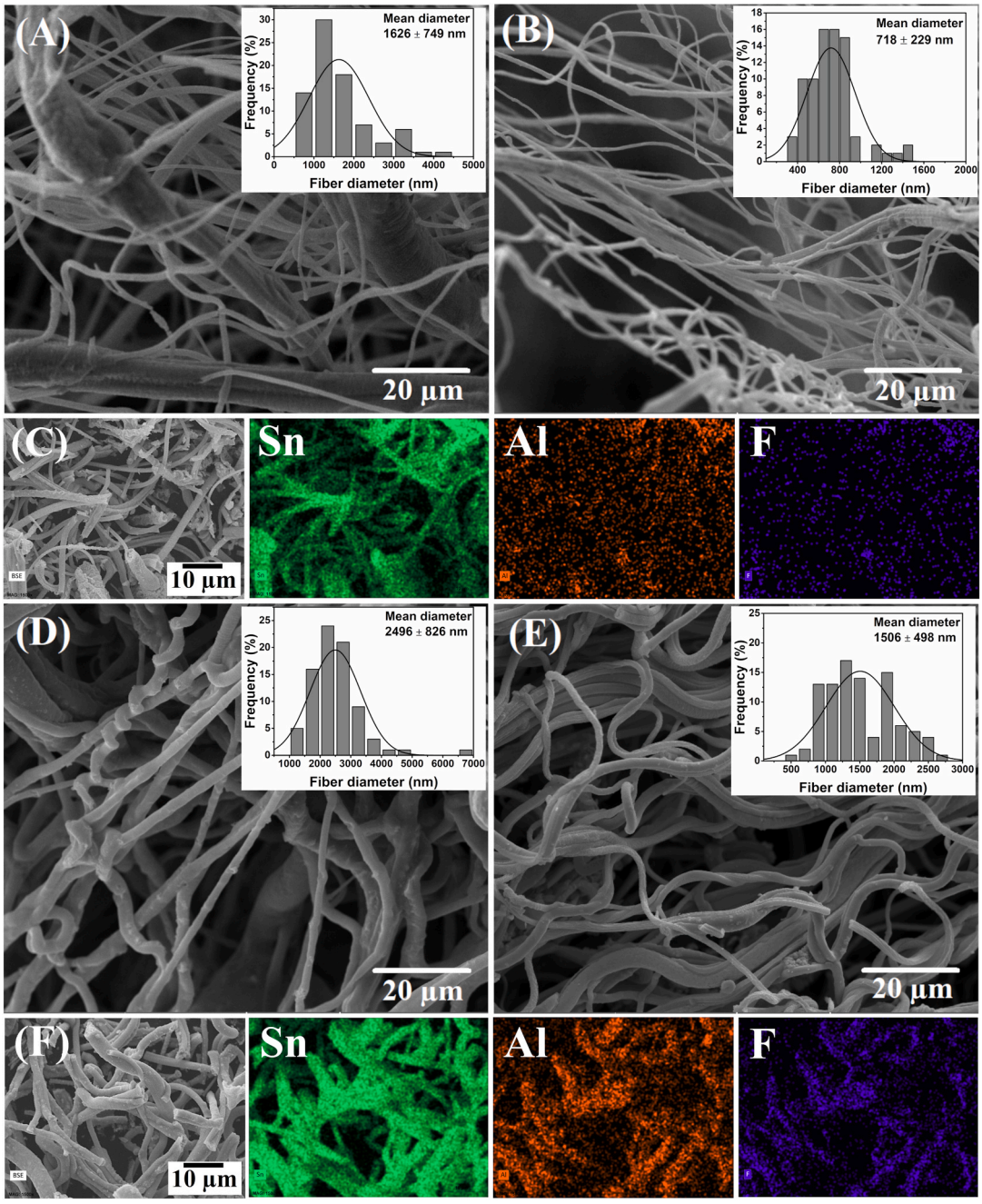

Fig. 3. SEM micrographs of (A) as-spun 1Al/15FTO fibers, (B) 1Al/15FTO fibers calcined at 600 °C, (C) X-ray fluorescence mapping of the 1Al/15FTO fibers, (D) as-spun 5Al/15FTO fibers, (E) 5Al/15FTO fibers calcined at 600 °C, and (E) X-ray fluorescence mapping of the 5Al/15FTO fibers.

5Al/15FTO fibers, respectively, that confirm the Al and F incorporation into the SnO_2 fibers. As can be seen, the elemental mapping shows a very uniform distribution of Al and F, which could indicate that the Al–SnO_2 and F–SnO_2 are well distributed and arranged in an entangled way.

Fig. 4A shows the XRD patterns of SnO_2, 15FTO and Al/FTO samples. The diffraction peaks can be indexed to the rutile-type tetragonal crystalline structure of tin dioxide (JCPDS data card No.41-1445), confirming the formation of a highly crystalline SnO_2 phase. The main XRD diffraction peaks are assigned to the (110), (101), (200) and (211) crystallographic planes. There are no peaks of impurity phases, suggesting that the doping elements have been incorporated into the SnO_2 lattice. A (110) peak shift to higher 2θ degrees (Fig. 4B) indicates the substitution of Sn^{4+} by Al^{3+} occurred within the lattice [31]. The peak shift is caused by increasing Al content, which leads to reduced interplanar d-spacing and the lattice parameters. In fact, a reduction in the lattice parameters was observed with increasing Al concentration (Table 1). The lattice parameters ***a*** and ***c*** were estimated by combining the following equations in the case of the tetragonal crystal system [32]:

$$n\lambda = 2d \sin\theta \tag{2}$$

$$\frac{1}{d} = \left(\frac{h^2 + k^2}{a^2} + \frac{l^2}{c^2}\right)^{\frac{1}{2}} \tag{3}$$

where d represents the interplanar distance, (hkl) are the miller indices of the (110) and (101) diffraction peaks, θ is Bragg's diffracting angle and λ is CuKα radiation wavelength ($\lambda = 1.5418$ Å). This procedure has been applied in the literature to estimate the lattice parameters of SnO_2 materials [33–35].

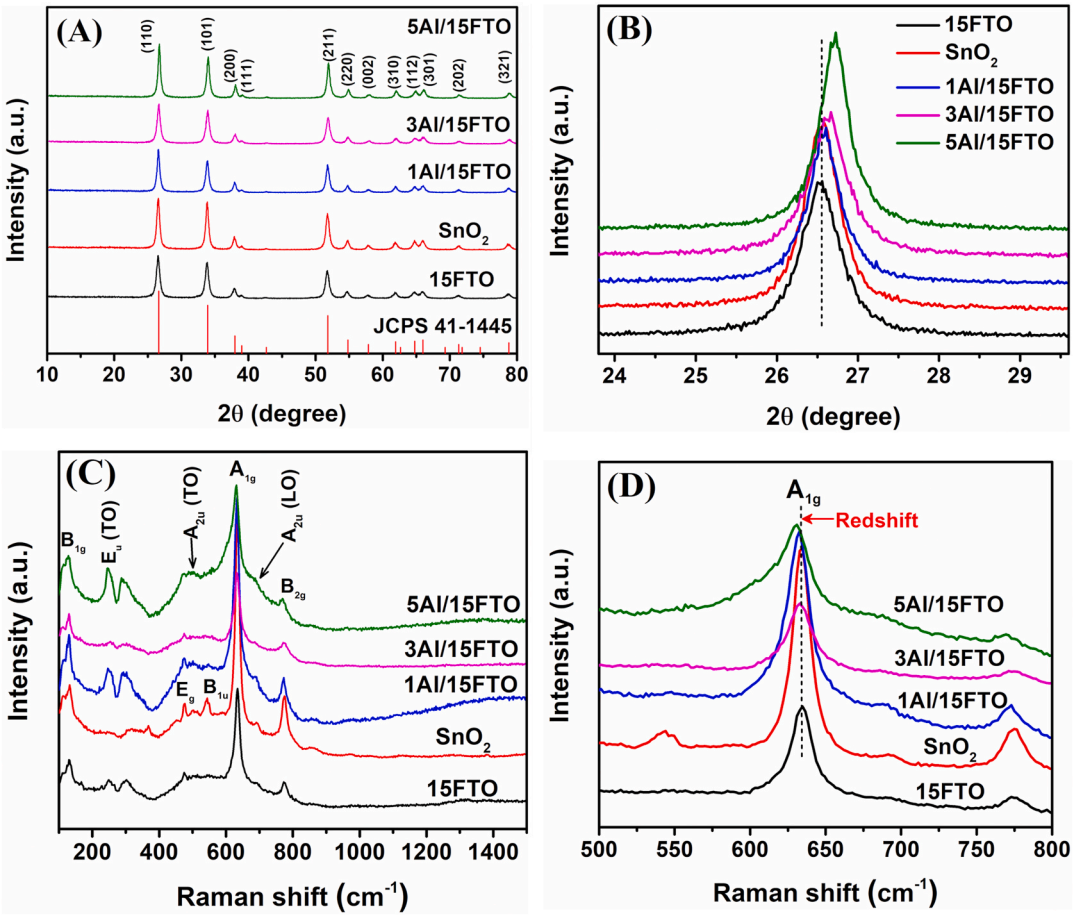

Fig. 4. (A) XRD patterns of pure SnO_2, 15FTO and Al/FTO fibers. (B) Shift of (110) peak to higher 2θ angles upon increasing Al content. (C) Raman spectra of SnO_2, 15FTO and Al/FTO fibers. (D) Redshift of the A_{1g} mode of all samples.

Table 1
Lattice parameters, unit cell volume and crystallite size of Al–SnO_2/F–SnO_2 fibers.

Lattice parameters				
	a (Å)	c(Å)	V (Å^3)	D (nm)
SnO_2	4.79	3.21	73.8	18
15FTO	4.75	3.19	72.1	17
1Al/15FTO	4.79	3.21	73.7	19
3Al/15FTO	4.78	3.21	73.3	17
5Al/15FTO	4.77	3.20	72.7	21

Lattice distortion was expected since Al and Sn have dissimilar atomic radii. The crystallite size was estimated using the strongest diffraction peak of (110) and by applying Debye Scherrer's equation

$$D = \frac{K\lambda}{\beta \cos\theta} \quad (4)$$

where D is the crystallite size, K is the shape constant, λ is CuKα radiation wavelength ($\lambda = 1.5418$ Å), β is the full width at half maximum (FWHM) in radian, and θ is Bragg's diffracting angle. The crystallite size results are shown in Table 1. No significant variation in crystallite size is observed with increasing Al e F content.

Raman scattering can be used to identify the crystal structure and study structural defects and size effects of nanocrystalline solids on the vibrational properties. The unit cell of SnO_2 possesses 6 atoms, giving a total of 18 vibrational modes in the first Brillouin's zone. The normal vibrational modes at the center of the Brillouin's zone are represented as: $\Gamma = A_{1g} + A_{2g} + B_{1g} + B_{2g} + E_g + A_{2u} + 2B_{1u} + 3E_u$. The A_{2g} and B_{1u} are not infrared (IR) and Raman active, while the A_{2u} and E_u are IR active and the remaining modes (A_{1g}, B_{1g}, B_{2g} and E_g) are all Raman active and represent fundamental vibrational modes of SnO_2-based materials [36–38]. The Raman spectra of pure, 15FTO and Al/FTO fibers are shown in Fig. 4C and confirm the formation of tetragonal rutile structure characteristic of tin dioxide [37], corroborating with the XRD results. The main Raman modes identified in all compositions were 113, 249, 475, 501, 543, 634, 691 and 775 cm^{-1}. The peak at 475 cm^{-1} is ascribed to the doubly degenerate E_g mode corresponding to the in-plane oxygen vibration. The Raman shifts at 634 cm^{-1} and 775 cm^{-1} are related to A_{1g} and B_{2g} non-degenerate modes that vibrate in a plane perpendicular to the c-axis and correspond to the vibrating expansion and contraction of the Sn–O bonds [39]. The red-shift and broadening of these Raman modes reflect the addition of F [40] and the increase in Al doping (Fig. 4D). For every 4 F^- that substitute O^{2-} in the lattice, a Sn vacancy ($V_{Sn}^{''''}$) may be created. Meanwhile, Al^{3+} substitutes Sn^{4+} positions in the lattice, likely generating oxygen vacancies. These defects appear in the material to ensure charge neutrality and are likely to form defect clusters. Surface defects cause lattice distortion at the interface and interior surface, reflecting in the Raman modes [41]. In disordered crystals, imperfections change the local symmetry, preventing atoms from vibrating in-phase and changing the components of the polarizability tensor [42]. As a result of surface defects and crystal disorder, Raman forbidden modes of E_u(TO), A_{2u}(TO), B_{1u} and A_{2u}(LO) at 248, 502, 544 and 694 cm^{-1}, respectively, and surface defect-related vibrational features at 400-700 cm^{-1} have been reported to appear in nanocrystalline SnO_2 materials along with the classical symmetry allowed Raman modes [42,43]. The Raman shifts observed at 250, 501, 543–547

and 691 cm^{-1} are ascribed to E_u(TO), A_{2u}(TO), B_{1u} and A_{2u}(LO) IR active (Raman forbidden) modes, and their presence evidence the local disorder promoted by surface defects (e.g., oxygen vacancies) and reduced particle effects. The decrease in Raman intensity upon doping also suggests that F and Al are responsible for the changes in lattice symmetry promoted by defects, which resulted in the appearance of Raman forbidden shifts [36,38]. Moreover, the particularly broad bands between 400 and 700 cm^{-1} observed in pure SnO_2, 15FTO and Al/FTO fibers are commonly encountered in the Raman spectrum of nanocrystalline SnO_2 [44]. These bands have been associated with low particle-sized materials that display increased sensitivity to various gases [41,43].

X-ray photoelectron spectra (XPS) measurements were performed to investigate the chemical states and the effect of F and Al doping on the as-prepared samples. Fig. 5A shows the survey XPS spectra of pure SnO_2, 1Al/15FTO and 5Al/15FTO samples. Peaks at binding energies corresponding to O, Sn, Al and C were clearly detected for all Al-doped samples. O 1s peaks are asymmetric, suggesting more than one chemical state of oxygen [40]. Shifts in the Sn 3d and O 1s states with the addition of F and Al dopants are observed, which could represent the effect of F^- and Al^{3+} incorporation in the lattice [40,45].

High-resolution XPS spectra show a more comprehensive analysis of the chemical states (Fig. 5B–D). The O 1s was deconvoluted with three peaks located at different binding energies. The peaks at binding energies between 530 eV and 531.5 eV are ascribed to oxygen in the SnO_2 crystal lattice (O_L) and correspond to Sn–O bonds (Fig. 5B). A decrease in the peak area upon F addition could indicate F^- substitution of O^{2-} in the lattice [40]. The redshift (about 0.7 eV) of the O 1s peak observed for the 5Al/15FTO spectrum could be indicative of Al incorporation. Peaks between 531.9 eV and 532.8 eV can be attributed to oxygen vacancies (O_V) present on the surface of the SnO_2 fibers [4,36]. However, peaks at higher binding energies between 533.2 and 533.9 eV are associated with chemisorbed oxygen species (O^- and O_2^- ions) [11]. The oxygen vacancy concentration varies from sample to sample, probably due to the heterogeneous nature of the hybrid fibers. We believe that the Al-doped fibers in the F–SnO_2/Al–SnO_2 hybrid contain more oxygen vacancies, giving the distinct oxidation states and atomic radius of Sn^{4+} and Al^{3+} ions. The presence of oxygen deficiencies and chemisorbed oxygen ions is readily beneficial for the gas sensing properties of SnO_2-based gas sensors. The oxygen defects are reactive sites for gas adsorption and contribute with free electrons, promoting the formation of more oxygen species on the surface [11]. These chemisorbed oxygen ions react with ethanol molecules, liberating electrons and decreasing sensor resistance. The Sn 3d high-resolution XPS spectra consist of doublet peaks (spin-orbit splitting) located in the range of 486.8–487.7 eV and 495.3–496.1 eV and assigned to Sn $3d_{5/2}$ and Sn $3d_{3/2}$, respectively (Fig. 5C). The separation of 8.45 eV between these two levels confirms the Sn^{4+} chemical state in the tetragonal structure of SnO_2 [36], further corroborating with the XRD and Raman results. In addition to these peaks, Al 2p peaks (Fig. 5D) are also observed in the XPS spectra of Al-doped samples. The binding energies located at 73.9 and 74.2 eV are related to Al $2p_{3/2}$ and Al $2p_{1/2}$ levels of Al^{3+} ions incorporated in the SnO_2 lattice [39,46]. The above results confirm that Al^{3+} ions have been successfully doped into the SnO_2 lattice. The absence of the F 1s level could be due to the low percentage (15 at%) of F^- in the compositions, which was not enough to generate a high signal/noise ratio. Wang et al.

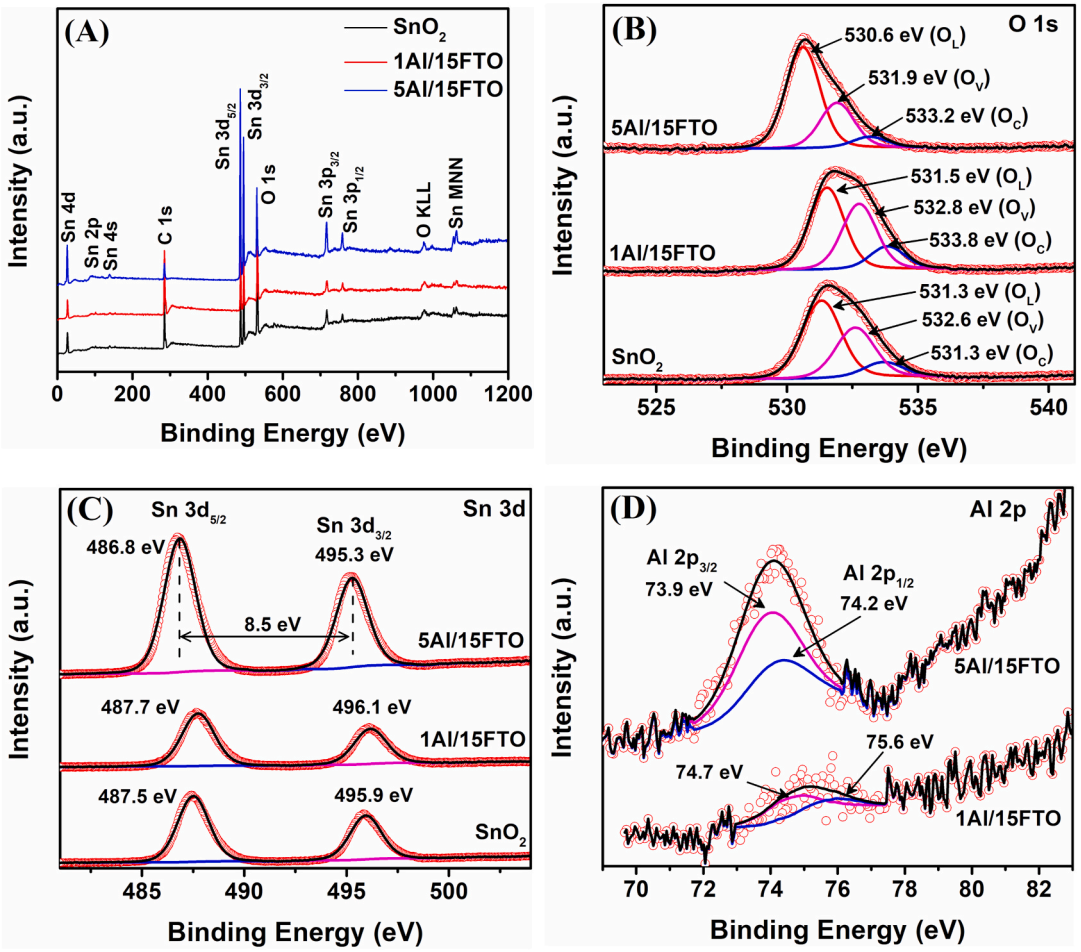

Fig. 5. (A) XPS survey spectra of SnO_2 and Al/FTO fibers. Gaussian deconvoluted XPS spectra of (B) O 1s, (C) Sn 3d, and (D) Al 2p chemical states of 5Al/15FTO fibers.

[36] barely detected the binding energy of the F 1s chemical state working with a much higher percentage of fluorine (50 at%), which almost disappeared with increasing the annealing temperature from 350 °C to 800 °C. XPS is a very surface-sensitive chemical analysis technique that can only detect electrons from only the top few atomic layers of the surface. The mean free path of electrons contributing to the XPS signal is tens of angstroms [47]. Furthermore, the high calcination temperature (600 °C) might have eliminated most of the light F^- ions from the surface of the fibers. These factors combined could explain the absence of the F 1s signal, even though fluorine has been detected by X-ray fluorescence mapping.

Fig. 6 shows the N_2 adsorption/desorption isotherms for the SnO_2, 15FTO, 1Al/15FTO and 5Al/15FTO samples. According to the IUPAC classification [48], the samples exhibit type IV isotherms with an H1-type hysteresis loop at high relative pressures. These isotherms with an abrupt increment in N_2 adsorption near $P/P_0 = 1$ are characteristic of highly mesoporous materials [48] and indicate capillary condensation within uniform pores [49,50]. Table 2 lists the BET-specific surface area, average pore diameter and pore volume of the fibers. The calculated BET surface areas are 4.3 m^2/g, 26.8 m^2/g, 11.4 m^2/g and 15.7 m^2/g for the SnO_2, 15FTO, 1Al/15FTO and 5Al/15FTO compositions, respectively. The variation in the surface area follows the pore volume values (see Table 2), with the 15FTO composition showing the highest pore volume and BET surface area among the samples. A similar observation was made by Zhao et al. [51]. The F-doped SnO_2 fibers show a larger BET-specific surface area than the blank sample (SnO_2), which is reduced upon simultaneous spinning with Al-doped SnO_2 fibers to form the Al/FTO compositions. Therefore, the main contribution to the high surface area in the hybrid Al–SnO_2/F–SnO_2 fibers is from the F–SnO_2 part. However, by increasing Al content in the Al-doped fibers, the surface area increased from 11.4 to 15.7 m^2/g. This indicates that Al^{3+} has a positive effect on the textural properties of SnO_2. The larger BET surface area of the doped samples is ascribed to the higher volume of mesopores shown in the pore size distribution (inset of Fig. 6). Ammonium fluoride (NH_4F) is known to generate porous hierarchical SnO_2 structures with large specific surface areas [52], which could be facilitated in acidic environments [53]. The formation of mesoporous materials in this work may have been influenced by the use of NH_4F in an acidic media (acetic acid). The mesoporous structure could also be explained by the release of gases during the decomposition of NH_4F and Al nitrate precursors. Furthermore, lattice distortion upon F and Al doping, evidenced by the decrease in lattice parameters (see Table 1), may also support the increase in the surface area observed. The highly mesoporous structure of the fibers can facilitate gas diffusion, resulting in higher and faster sensing responses [54].

Table 2
– BET surface area, pore diameter and pore volume for the SnO_2, 15FTO, 1Al/15FTO and 5Al/15FTO fibers.

	Sample			
	SnO_2	15FTO	1Al/15FTO	5Al/15FTO
Specific surface area (m^2/g)	4.3	26.8	11.4	15.7
Average pore diameter (nm)	–	25.3	24.2	27.6
Pore volume (cm^3/g)	0.026	0.131	0.066	0.102

3.2. Ethanol gas-sensing properties of Al/FTO samples

The current-voltage studies (I–V) of pure SnO_2, 15FTO and Al/FTO samples were performed on thin-film sensors prepared by dispersing the fibers in isopropyl alcohol and depositing them onto a pair of copper electrodes. The measurements have been carried out in the current range

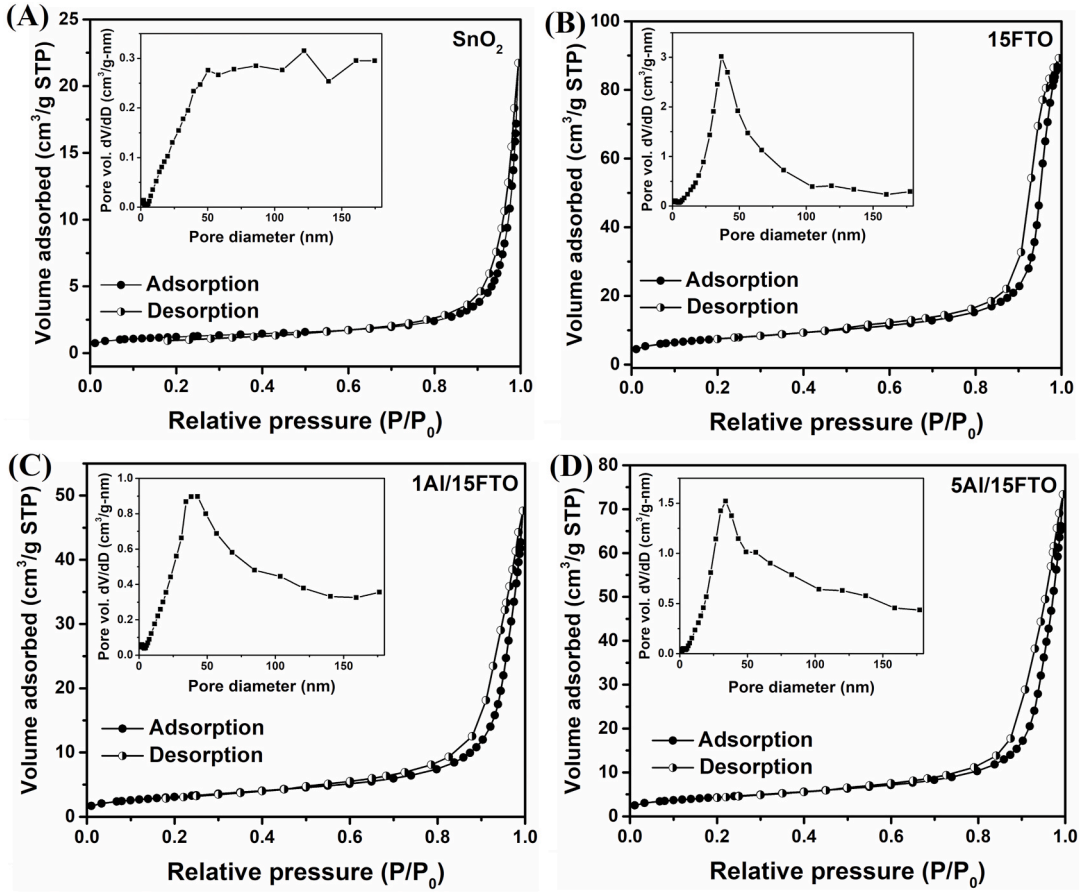

Fig. 6. N_2 adsorption/desorption isotherm and BJH pore size distribution curves (inset) of: SnO_2 (A), 15FTO (B), 1Al/15FTO (C), and 5Al/15FTO (D) hybrid fibers.

of −0.8 μA to +0.8 μA under ambient conditions (50%RH and 25 °C). Interestingly, the I–V curves (Fig. 7A) showed a sigmoidal-like behavior with a linear region in the center. The contact between the metal electrodes and the n-type semiconductor is expected to show a Schottky behavior in the air [55], explaining the non-linearity for higher forward and reversed bias. The samples behave as a p-n junction diode, showing reversible I–V curve characteristics. The linear portion of the curves shows the good ohmic conducting behavior [56] often desired for gas sensing applications. The I–V characteristic curves of the 15FTO and 5Al/15FTO samples are considerably more inclined towards the middle axis, which means that a higher current is achieved for the same applied voltage compared to the other compositions. Therefore, these compositions present the highest conductivity among the samples tested. The conductivity increased with F and Al addition to SnO_2 and by preparing F–SnO_2/Al–SnO_2 hybrid fibers. The enhanced conductivity could also be due to the increased charge transfer between the F–SnO_2 and Al–SnO_2 fibers facilitated by the fibrillar morphology and intimate contact between fibers.

The gas-sensing performance of the Al–SnO_2/F–SnO_2 fibers was studied by performing tests with ethanol vapors. Fig. 7B–F shows the resistance as a function of time for the SnO_2, 15FTO and Al/FTO-based gas sensors. The tests were carried out at room temperature (RT) using ethanol concentrations ranging from 10 to 100 ppm. When ethanol was injected into the test chamber, the resistance decreased quickly and reached a certain level (saturation) after a period that depended on the gas concentration. When the test chamber opened, the sensor recovered its initial resistance. This behavior implies an n-type semiconductivity of the sensing material [6]. As can be seen, the base resistance of the sensors decreased as the amount of dopant increased, in agreement with the current-voltage (I–V) results. The 15FTO (15 at% F) composition showed the lowest base resistance. As reported in previous work [10], by doping SnO_2 with fluorine, a drop in the resistance of SnO_2 fibers takes place due to free electron generation. The parallel spinning of Al-doped and F-doped led to higher base resistances when compared to the 15FTO samples. This is ascribed to the higher resistance of the Al-doped fibers that compose part of the Al–SnO_2/F–SnO_2 hybrid system. However, a drastic drop in base resistance as the Al content increased from 1.0 at% to 5.0 at% in the hybrid might suggest the presence of oxygen vacancies (shallow electron donors), introduced by Al^{3+} substitution of Sn^{4+} ions in the lattice, as also suggested by the XPS results. The sample containing more Al (5 at%) displayed lower initial resistance among the hybrid Al/FTO fibers and a more significant resistance change when ethanol was injected into the testing chamber. Therefore, the 5Al/15FTO composition presented the highest sensitivity towards ethanol at RT among all samples tested (Fig. 8A). Interestingly, the 15FTO fibers alone displayed a higher ethanol sensing response than the 1Al/15FTO and 3Al/15FTO sensors. The high specific surface area (26.8 m^2/g) coupled with F doping is likely the reason for the elevated ethanol sensitivity of the 15FTO sample. Nevertheless, the 5Al/15FTO hybrid fibrous system demonstrated superior performance, with high sensitivity, selectivity and long-term stability, and, hence, presents a potential for application in real-life ethanol sensing devices. The maximum response obtained for the 5Al/15FTO sensor was 3.0–100 ppm ethanol at RT (9 times higher than the pure SnO_2 sensor). Table 3 compares the results found in this work and others reported in the literature. The sensing response of this work is comparable or even higher than other results found in the literature, especially considering that the optimized response in most cases is obtained at a high working temperature [15,27]. High temperatures facilitate gas adsorption and oxidation, enhancing the sensing response.

Other key parameters in evaluating the practical application of solid-state gas sensors are the response/recovery times, repeatability, long-term stability and selectivity. These parameters were studied for the 5Al/15FTO sensor, which showed the best sensing results among the sensors tested. Fig. 8B shows the response-recovery curve of the 5Al/15FTO sensor towards 80 ppm ethanol. The response-recovery time is 125 s and 162 s, respectively. The result indicates that the 5Al/15FTO-based gas sensor presents fast response and recovery rates, critical for low working temperature sensors. The continuous fiber structure and the interface interaction between Al-doped and F-doped SnO_2 fibers may

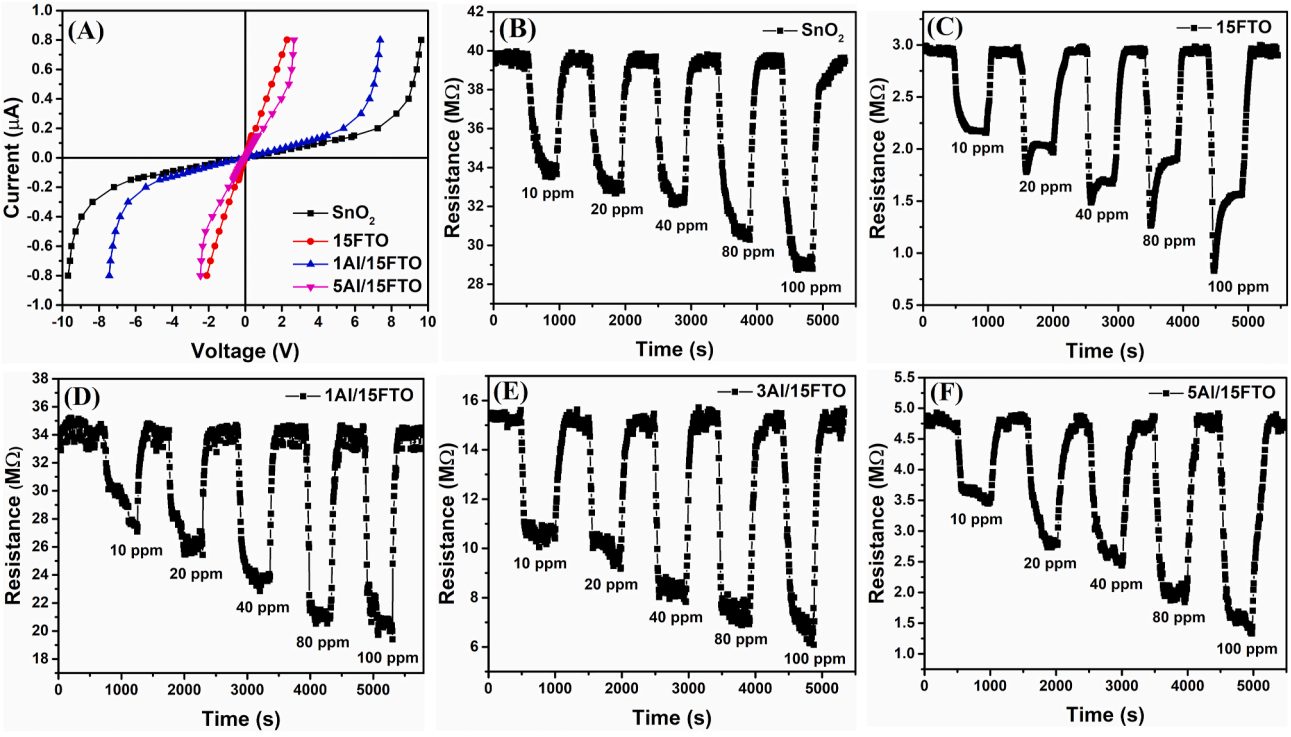

Fig. 7. (A) I–V curves of SnO_2, 15FTO and Al/FTO based gas sensors at 25 °C. Resistance transient curves of pure SnO_2 (B), 15FTO (C), 1Al/15FTO (D), 3Al/15FTO (E), and 5Al/15FTO (F) towards different concentrations of ethanol at RT.

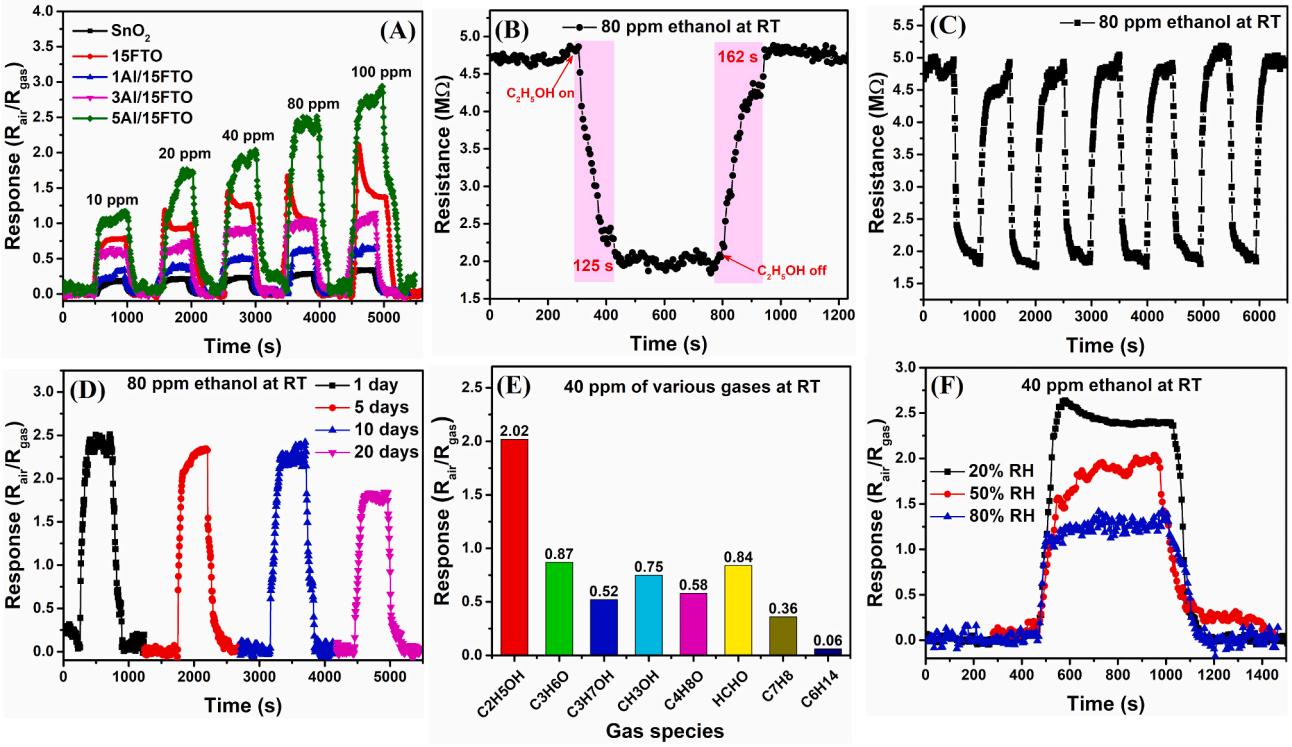

Fig. 8. (A) Response vs time curves of the Al/FTO-based gas sensors to ethanol at RT. (B) Response and recovery times of the 5Al/15FTO fibers to 40 ppm ethanol at RT. (C) Cycling of the 5Al/15FTO based sensor for 80 ppm ethanol. (D) Long-term cycling stability of the 5Al/15FTO for 20 days. (E) Sensitivity of the 5Al/15FTO sensor to 40 ppm of various gases at RT. (F) 5Al/15FTO sensor response towards 40 ppm ethanol at 20, 50 and 80% RH.

Table 3
Comparison of sensing response and response/recovery times of various gas sensors towards ethanol.

Materials	Concentration (ppm)	Response (R_{air}/R_{gas})	Temperature (°C)	Resp/rec time (s)	Reference
Fluorinated MWCNTs	50	1.13	RT	95/227	[57]
SnO_2 nanowires	100	1.38	400	–	[58]
Pr-SnO_2 nanofibers	100	28	300	116/11	[59]
Zn–SnO_2 hierarchical architectures	100	14	213	30/160	[60]
Horseshoe-shaped SnO_2	100	17.3	225	8/780	[61]
$NiCo_2O_4$@SnO_2 heterostructure nanofiber	100	8.87	160	–	[15]
Nanogap sensors decorated with SnO_2 NPs	10	17.9	100	85/5132	[62]
Pd–SnO_2 thin films	120	3.5	RT	107/378 (40 ppm)	[14]
SnO_2-rGO composite	58	2.1	RT	123/128	[63]
Al–SnO_2/F–SnO_2 fibers	100	3.0	RT	125/162 (80 ppm)	This work

have aided electron transfer, facilitating ethanol oxidation at RT and resulting in enhanced sensing response. The presence of oxygen vacancies and F^- and Al^{3+} incorporation in the lattice resulted in better conductivity and improved surface reactive sites that helped enhance sensitivity and response/recovery rates [4]. Moreover, fluorine atoms are more electronegative and attract ethanol molecules, promoting a faster response time. Simultaneously, fluorine forms a weak hydrogen bond with ethanol during adsorption, which provides a quicker recovery [57]. Solid-state gas sensors with fast response-recovery rates at low working temperatures have also been reported in the literature [11,13]. Compared to previously reported results for ethanol sensing (Table 3), the co-spun Al–SnO_2/F–SnO_2 fibers show improved response/recovery times for low operating gas sensors.

The repeatability was evaluated by exposing the 5Al/15FTO sensor to 80 ppm ethanol (Fig. 8C). After several cycles of ethanol exposure, the sensor maintains its initial response amplitude without significant attenuation of the signal. Fig. 8D exhibits the sensor response towards 80 ppm ethanol at RT over a period of 20 days. As can be seen, the sensor preserves a good level of sensitivity during the period evaluated and, therefore, shows long-term stability, desired in the development of functional gas sensors. The result demonstrates the stability of the Al/FTO sensor and further supports the robustness of the sensing material prepared in the present work. The selectivity towards ethanol was evaluated by performing sensing tests with 40 ppm of many volatiles, including ethanol, acetone, isopropanol, methanol, methyl ethyl ketone, formaldehyde, toluene and hexane. Fig. 8E shows the response/recovery curves for all gases tested. As can be seen, the 5Al/15FTO sample presents higher sensitivity towards ethanol and, thus, demonstrates selectivity to this volatile.

The influence of the relative humidity on the sensitivity of a solid-state gas sensor is a critical factor to be studied [64,65] since in real-life conditions the relative humidity can vary during different times of the day and seasons of the year. Fig. 8F shows the response curves of the 5Al/15FTO sensor under varying RH conditions at RT. As the humidity increases, the response signal diminishes, demonstrating the prejudicial effect of humidity on the sensitivity of the SnO_2-based gas sensors. The reduction in sensitivity under high RH is explained by the competition for active sites between water and ethanol molecules taking place on the surface of the sensing material [10,11]. The ending result is the occupation of part of the active sites by these water molecules,

reducing the adsorption and further oxidation of ethanol on the surface.

3.3. Ethanol gas sensing mechanism

Fig. 9 illustrates the sensing mechanism of the fibers towards ethanol gas. The surface depletion model is often applied to describe the gas sensing mechanism of SnO_2-based sensors [8,9]. In this model, supported by experimental observations, the atmospheric oxygen adsorbs on the surface of SnO_2 and captures electrons of the conduction band, forming reactive oxygen species, such as O^{2-}, O_2^- and O^-. The oxygen chemisorption at temperatures below 160 °C occurs mainly through the formation of O_2^- [59]. An electron-depleted zone is formed on each grain surface with a consequent increase in electrical resistance. Upon exposure to a reducing gas (e.g., ethanol), a reaction occurs between the target gas molecules and the adsorbed oxygen species, releasing the trapped electrons back to the conduction band. The interaction with the reducing gas decreases the electrical resistance of the sensing material. The interaction between oxygen and the target gas depends on the type of gas and its affinity with oxygen; in this case, the reaction rate is decisive in the response and recovery times. The chemisorptions of oxygen species and ethanol oxidation at low temperatures can be described as follows [60]:

$$O_2 \rightarrow O_2(ads) \quad (5)$$

$$O_2(ads) + e^- \rightarrow 2O_2^-(ads) \quad (6)$$

$$2C_2H_5OH(ads) + O_2^-(ads) \rightarrow 2CH_3CHO + 2H_2O(gas) + e^- \quad (7)$$

Despite the large diameter, the Al/FTO hybrid fibers sustain a good ethanol sensing performance at room temperature (25 °C). The synergistic effect between the long-range fiber structure, Al and F doping, the high specific surface area and the interaction between the Al-doped and F-doped SnO_2 fibers favored gas diffusion, electron transport and oxygen adsorption, resulting in improved sensing response. The replacement of Sn^{4+} by Al^{3+} in the SnO_2 lattice introduces an electronic hole, and the Al^{3+} cation acts as an acceptor impurity [66]. This reaction occurs as follows:

$$Al_{Sn} \rightarrow Al_{Sn}^{'} + h^+ \quad (8)$$

Electron holes capture electrons from the sensor, decreasing charge carrier concentration and increasing the depletion layer between grains. Such an effect was reported by Wu et al. [31] for Al atomic fractions below 4%. However, for Al atomic percentages between 4% and 8%, a decrease in resistance was observed, which was associated with the formation of oxygen vacancies ($V_O^{\bullet\bullet}$). $V_O^{\bullet\bullet}$ acts as electron-donating impurities and increases the conductivity of SnO_2. The formation of oxygen vacancies by Al doping is represented by:

$$Al_{Sn} + O_O \xrightarrow{SnO_2} Al_{Sn}^{'} + V_O^{\bullet\bullet} + 1/2O_2 + e^{'} \quad (9)$$

Each oxygen vacancy donates two electrons as follows:

$$O_O^x \rightarrow V_O^{\bullet\bullet} + 1/2O_2 + 2e^{'} \quad (10)$$

Therefore, although the Al^{3+} ions introduce electron holes, the number of electrons generated exceeds that of holes and the net effect is an increased conductivity [31]. Oxygen vacancies also function as reactive sites, wherein oxygen adsorbs and reacts with the surface, contributing to enhanced sensing response [2,11].

Doping with fluorine, in turn, leads to an increase in the concentration of free electrons in a process that can be represented by:

$$O_O^x \rightarrow F_O^{\bullet} + 1/2O_2 + e^- \quad (11)$$

For the Al–SnO_2/F–SnO_2 hybrid-like fibers, the improved sensing response at room temperature may be due to the combined effect of Al and F dopants, which increased charge carrier concentration and improved electron transport properties. The Al^{3+} doping possibly introduced several defects due to the different valence states of Al^{3+} and Sn^{4+} ions, as demonstrated by the XPS data. The most important surface defects for gas sensing are undoubtedly oxygen-vacant sites, which are the main active centers for oxygen adsorption since such defects are electron donors in nature. On the other hand, F^- ion in the SnO_2 lattice leads to the formation of n-type semiconductors, dramatically increasing SnO_2 conductivity. This is because F^- replaces O^{2-} in the crystal lattice due to the similarity of electronegativities and anion sizes [67]. F^- has one extra valence electron weakly bound to the lattice that strongly contributes to the conductivity. The high conductivity, facilitated by electron transfer across the entire fiber-mat, enhances oxygen adsorption, widening the electron depletion region. This leads to an even greater difference in electrical resistance before and after ethanol exposure. When ethanol is injected into the test chamber, the gas molecules react with oxygen ions at the Al–SnO_2/F–SnO_2 surface, releasing the trapped electrons and decreasing sensor resistance. Furthermore, materials with high specific surface areas provide more active sites for oxygen adsorption, which contributes to a larger electron-depleted layer and, consequently, improves the gas sensing properties [68]. The Al/FTO fibers produced by parallel-SBS presented high BET surface area and a mesoporous structure. These properties were partly responsible for promoting gas diffusion (oxygen and ethanol) and oxygen adsorption; thereby, leading to the high sensing performance to ethanol at room temperature.

The importance of this work relies on the fact that it provides a very simple way of producing highly functional hybrid/composite

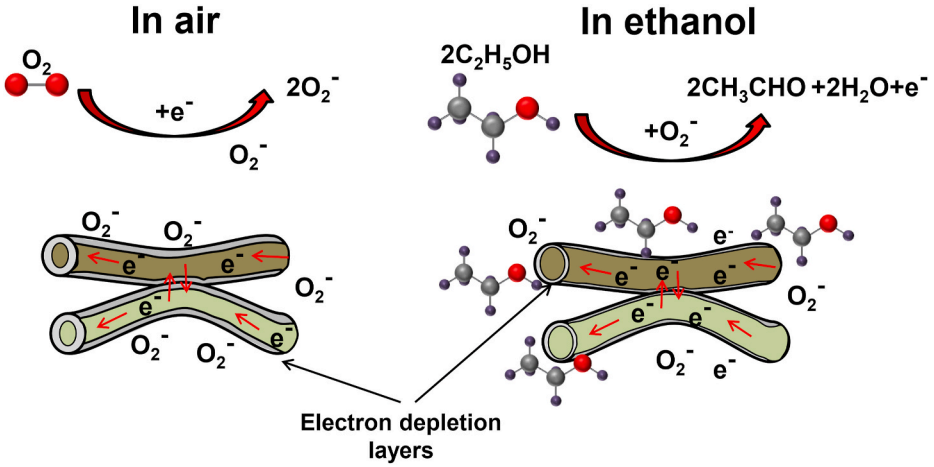

Fig. 9. Schematic illustration of the gas sensing mechanism of Al/FTO fibers.

nanomaterials for application in gas sensors and other similar important applications using the SBS technique. More importantly, the good sensing performance to ethanol gas at room temperature presented by the Al–SnO_2/F–SnO_2 fibers indicates a potential use of such material in real-life gas sensors applied, for instance, in breath analyzers.

4. Conclusion

Al–SnO_2/F–SnO_2 fibers were successfully spun simultaneously by the Solution Blow Spinning method followed by heat treatment at 600 °C. The calcination at 600 °C converted the fibers into the desired SnO_2 phase by volatilization of the organic compounds. The XRD, Raman spectroscopy and XPS results confirmed the formation of a highly crystalline tetragonal SnO_2 phase. The influence of doping elements was evidenced by the presence of Al 2p and oxygen vacancy-related peaks in the XPS spectra and by X-ray fluorescence mapping. The N_2 adsorption/desorption analysis showed a large pore size and large BET-specific surface area for the samples. The mesoporous structure and the large surface area of the fibers effectively contributed to the high sensitivity to ethanol at room temperature. The conductivity and ethanol sensing properties of the hybrid Al–SnO_2/F–SnO_2 fibers were efficiently improved by the synergistic effect of Al and F doping, which increased surface ($V_O^{\bullet\bullet}$) and electronic (e^-) defects and promoted better electron transport and oxygen adsorption. The Al–SnO_2/F–SnO_2 composites showed promising results in the detection of ethanol at room temperature.

Declaration of competing interest

The authors declare that they have no known competing financial interests or personal relationships that could have appeared to influence the work reported in this paper.

Acknowledgments

This work was supported by the Coordenação de Aperfeiçoamento de Pessoal de Nível Superior – Brazil [Finance Code 001 – scholarship granted to Mr. Emanuel P. Nascimento] and the National Council for Scientific and Technological Development – CNPq [grant nos. 308822/2018-8 and 420004/2018-1]. Francisco J. A. Loureiro is thankful for the Investigator Grant CEECIND/02797/2020 and the projects UIDB/00481/2020, UIDP/00481/2020, and CENTRO-01-0145-FEDER-022083 - Centro Portugal Regional Operational Programme (Centro2020), under the PORTUGAL 2020Partnership Agreement, through the European Regional Development Fund (ERDF).

References

[1] J.H. Bang, N. Lee, A. Mirzaei, M.S. Choi, H.S. Choi, H. Park, H. Jeon, S.S. Kim, H. W. Kim, SnS-functionalized SnO_2 nanowires for low-temperature detection of NO_2 gas, Mater. Char. 175 (2021), 110986, https://doi.org/10.1016/j.matchar.2021.110986.

[2] M. Shao, J. Liu, W. Ding, J. Wang, F. Dong, J. Zhang, Oxygen vacancy engineering of self-doped SnO_{2-x} nanocrystals for ultrasensitive NO_2 detection, J. Mater. Chem. C 8 (2020) 487–494, https://doi.org/10.1039/C9TC05705F.

[3] K.-C. Hsu, T.-H. Fang, I.-T. Tang, Y.-J. Hsiao, C.-Y. Chen, Mechanism and characteristics of Au-functionalized SnO_2/In_2O_3 nanofibers for highly sensitive CO detection, J. Alloys Compd. 822 (2020), 153475, https://doi.org/10.1016/j.jallcom.2019.153475.

[4] Q. Zeng, Y. Cui, L. Zhu, Y. Yao, Increasing oxygen vacancies at room temperature in SnO_2 for enhancing ethanol gas sensing, Mater. Sci. Semicond. Process. 111 (2020), 104962, https://doi.org/10.1016/j.mssp.2020.104962.

[5] Y. Xu, L. Zheng, C. Yang, X. Liu, J. Zhang, Highly sensitive and selective electronic sensor based on Co catalyzed SnO_2 nanospheres for acetone detection, Sensor. Actuator. B Chem. 304 (2020), 127237, https://doi.org/10.1016/j.snb.2019.127237.

[6] S. Singh, S. Kumar, S. Sharma, Room temperature high performance ammonia sensor using MoS_2/SnO_2 nanocomposite, Mater. Today Proc. 28 (2020) 52–55, https://doi.org/10.1016/j.matpr.2020.01.208.

[7] K. Hu, F. Wang, Z. Shen, H. Liu, W. Zeng, Y. Wang, Ar plasma treatment on ZnO–SnO_2 heterojunction nanofibers and its enhancement mechanism of hydrogen gas sensing, Ceram. Int. 46 (2020) 21439–21447, https://doi.org/10.1016/j.ceramint.2020.05.242.

[8] S. Bai, W. Guo, J. Sun, J. Li, Y. Tian, A. Chen, R. Luo, D. Li, Synthesis of SnO_2–CuO heterojunction using electrospinning and application in detecting of CO, Sensor. Actuator. B Chem. 226 (2016) 96–103.

[9] J. Hu, J. Yang, W. Wang, Y. Xue, Y. Sun, P. Li, K. Lian, W. Zhang, L. Chen, J. Shi, Synthesis and gas sensing properties of NiO/SnO_2 hierarchical structures toward ppb-level acetone detection, Mater. Res. Bull. 102 (2018) 294–303, https://doi.org/10.1016/j.materresbull.2018.02.006.

[10] E.P. Nascimento, H.C. Firmino, A.M. Santos, H.B. Sales, V.D. Silva, D.A. Macedo, G. A. Neves, E.S. Medeiros, R.R. Menezes, Facile synthesis of hollow F-doped SnO_2 nanofibers and their efficiency in ethanol sensing, J. Am. Ceram. Soc. 104 (2021) 1297–1308, https://doi.org/10.1111/jace.17580.

[11] L. Zhang, R. Tong, W. Ge, R. Guo, S.E. Shirsath, J. Zhu, Facile one-step hydrothermal synthesis of SnO_2 microspheres with oxygen vacancies for superior ethanol sensor, J. Alloys Compd. 814 (2020), 152266, https://doi.org/10.1016/j.jallcom.2019.152266.

[12] J.P. Cheng, J. Wang, Q.Q. Li, H.G. Liu, Y. Li, A review of recent developments in tin dioxide composites for gas sensing application, J. Ind. Eng. Chem. (Seoul, Repub. Korea) 44 (2016) 1–22, https://doi.org/10.1016/j.jiec.2016.08.008.

[13] R.J. Wu, D.J. Lin, M.R. Yu, M.H. Chen, H.F. Lai, Ag@SnO_2 core–shell material for use in fast-response ethanol sensor at room operating temperature, Sensor. Actuator. B Chem. 178 (2013) 185–191, https://doi.org/10.1016/j.snb.2012.12.052.

[14] V. Dhongade, L. Sharma, A. Kahandal, R. Aiyer, K. Rajdeo, C. Tagad, Pd doped SnO_2 based room temperature operable resistive sensor for the detection of ethanol vapors, Mater. Today Proc. 46 (2021) 1–3, https://doi.org/10.1016/j.matpr.2020.12.973.

[15] Q. Wang, J. Bai, B. Huang, Q. Hu, X. Cheng, J. Li, E. Xie, Y. Wang, X. Pan, Design of $NiCo_2O_4$@SnO_2 heterostructure nanofiber and their low temperature ethanol sensing properties, J. Alloys Compd. 791 (2019) 1025–1032, https://doi.org/10.1016/j.jallcom.2019.03.364.

[16] S. Dmitriev, Y. Lilach, B. Button, M. Moskovits, A. Kolmakov, Nanoengineered chemiresistors: the interplay between electron transport and chemisorption properties of morphologically encoded SnO_2 nanowires, Nanotechnology 18 (2007), 055707, https://doi.org/10.1088/0957-4484/18/5/055707.

[17] X. Bai, H. Lv, Z. Liu, J. Chen, J. Wang, B. Sun, Y. Zhang, R. Wang, K. Shi, Thin-layered MoS_2 nanoflakes vertically grown on SnO_2 nanotubes as highly effective room-temperature NO_2 gas sensor, J. Hazard Mater. 416 (2021), 125830, https://doi.org/10.1016/j.jhazmat.2021.125830.

[18] E.P. Nascimento, H.C.T. Firmino, G.A. Neves, R.R. Menezes, A review of recent developments in tin dioxide nanostructured materials for gas sensors, Ceram. Int. (2021), https://doi.org/10.1016/j.ceramint.2021.12.123. In press.

[19] R. Araujo, E. Nascimento, H. Firmino, D. Macedo, G. Neves, M. Morales, R. Menezes, α-Fe_2O_3 fibers: an efficient photocatalyst for dye degradation under visible light, J. Alloys Compd. 882 (2021), 160683, https://doi.org/10.1016/j.jallcom.2021.160683.

[20] H.C. Firmino, E.P. Nascimento, R.F. Bonan, P.P. Maciel, L.R. Castellano, L. N. Santana, G.A. Neves, R.R. Menezes, Antifungal activity of TiO_2-CeO_2 nanofibers against Candida fungi, Mater. Lett. 283 (2021), 128709, https://doi.org/10.1016/j.matlet.2020.128709.

[21] V.D. Silva, E.P. Nascimento, J.P. Grilo, T.A. Simões, R.R. Menezes, D.A. Macedo, E. S. Medeiros, Effect of two-step calcination on the formation of nickel oxide hollow nanofibers, Open Ceramics 5 (2021), 100087, https://doi.org/10.1016/j.oceram.2021.100087.

[22] R. Araujo, E. Nascimento, R. Raimundo, D. Macedo, V. Mastelaro, G. Neves, M. Morales, R. Menezes, Hybrid hematite/calcium ferrite fibers by solution blow spinning: microstructural, optical and magnetic characterization, Ceram. Int. 47 (2021) 33363–33372, https://doi.org/10.1016/j.ceramint.2021.08.239.

[23] Y.-J. Lee, H.-J. Ahn, Fabrication of uniform SnO_2–SiO_2–Pt composite nanofibres via co-electrospinning, Ceram. Int. 39 (2013) 5303–5308, https://doi.org/10.1016/j.ceramint.2012.12.033.

[24] B. Pal, Z.H. Bakr, S.G. Krishnan, M.M. Yusoff, R. Jose, Large scale synthesis of 3D nanoflowers of SnO_2/TiO_2 composite via electrospinning with synergistic properties, Mater. Lett. 225 (2018) 117–121, https://doi.org/10.1016/j.matlet.2018.04.120.

[25] F. Li, H. Song, W. Yu, Q. Ma, X. Dong, J. Wang, G. Liu, Electrospun TiO_2//SnO_2 janus nanofibers and its application in ethanol sensing, Mater. Lett. 262 (2020), 127070, https://doi.org/10.1016/j.matlet.2019.127070.

[26] E.S. Medeiros, G.M. Glenn, A.P. Klamczynski, W.J. Orts, L.H.C. Mattoso, Solution blow spinning: a new method to produce micro- and nanofibers from polymer solutions, J. Appl. Polym. Sci. 113 (2009) 2322–2330, https://doi.org/10.1002/app.30275.

[27] Q. Chen, S.Y. Ma, X.L. Xu, H.Y. Jiao, G.H. Zhang, L.W. Liu, P.Y. Wang, D. J. Gengzang, H.H. Yao, Optimization ethanol detection performance manifested by gas sensor based on In_2O_3/ZnS rough microspheres, Sensor. Actuator. B Chem. 264 (2018) 263–278, https://doi.org/10.1016/j.snb.2018.02.172.

[28] C. Wang, Z.G. Wang, R. Xi, L. Zhang, S.H. Zhang, L.J. Wang, G.B. Pan, In situ synthesis of flower-like ZnO on GaN using electrodeposition and its application as ethanol gas sensor at room temperature, Sensor. Actuator. B Chem. 292 (2019) 270–276, https://doi.org/10.1016/j.snb.2019.04.140.

[29] G.R. Ferreira, T. Segura, F.G. de Souza Jr., A.P. Umpierre, F. Machado, Synthesis of poly (vinyl acetate)-based magnetic polymer microparticles, Eur. Polym. J. 48 (2012) 2050–2069, https://doi.org/10.1016/j.eurpolymj.2012.09.003.

[30] L. Wang, H. Liu, J. Zhao, X. Zhang, C. Zhang, G. Zhang, Q. Liu, H. Duan, Enhancement of charge transport in porous carbon nanofiber networks via ZIF-8-

enabled welding for flexible supercapacitors, Chem. Eng. J. 382 (2019), 122979, https://doi.org/10.1016/j.cej.2019.122979.
[31] J. Wu, Q. Huang, D. Zeng, S. Zhang, L. Yang, D. Xia, Z. Xiong, C. Xie, Al-doping induced formation of oxygen-vacancy for enhancing gas-sensing properties of SnO_2 NTs by electrospinning, Sensor. Actuator. B Chem. 198 (2014) 62–69, https://doi.org/10.1016/j.snb.2014.03.012.
[32] B.D. Cullity, Elements of X-Ray Diffraction, second ed., Addison-Wesley Publishing, Massachusetts, 1956.
[33] V.S. Anitha, S. Sujatha Lekshmy, K. Joy, Effect of Mn doping on the structural, magnetic, optical and electrical properties of ZrO_2–SnO_2 thin films prepared by sol–gel method, J. Alloys Compd. 675 (2016) 331–340, https://doi.org/10.1016/j.jallcom.2016.03.045.
[34] F. Yang, Z. Guo, Comparison of the enhanced gas sensing properties of tin dioxide samples doped with different catalytic transition elements, J. Colloid Interface Sci. 448 (2015) 265–274, https://doi.org/10.1016/j.jcis.2015.02.045.
[35] W. Zhang, B. Yang, J. Liu, X. Chen, X. Wang, C. Yang, Highly sensitive and low operating temperature SnO_2 gas sensor doped by Cu and Zn two elements, Sensor. Actuator. B Chem. 243 (2017) 982–989, https://doi.org/10.1016/j.snb.2016.12.095.
[36] X. Wang, M. Xu, L. Liu, Y. Cui, H. Geng, H. Zhao, B. Liang, J. Yang, Effects specific surface area and oxygen vacancy on the photocatalytic properties of mesoporous F doped SnO_2 nanoparticles prepared by hydrothermal method, J. Mater. Sci. Mater. Electron. 30 (2019) 16110–16123, https://doi.org/10.1007/s10854-019-01981-y.
[37] A. Azam, A.S. Ahmed, S.S. Habib, A. Naqvi, Effect of Mn doping on the structural and optical properties of SnO_2 nanoparticles, J. Alloys Compd. 523 (2012) 83–87, https://doi.org/10.1016/j.jallcom.2012.01.072.
[38] J. Kaur, J. Shah, R. Kotnala, K.C. Verma, Raman spectra, photoluminescence and ferromagnetism of pure, Co and Fe doped SnO_2 nanoparticles, Ceram. Int. 38 (2012) 5563–5570, https://doi.org/10.1016/j.ceramint.2012.03.075.
[39] P.V. Reddy, S.V. Reddy, B.S. Reddy, Synthesis and properties of (Fe, Al) co-doped SnO_2 nanoparticles, Mater, Today Proc 3 (2016) 1752–1761, https://doi.org/10.1016/j.matpr.2016.04.070.
[40] X. Wang, X. Wang, Q. Di, H. Zhao, B. Liang, J. Yang, Mutual effects of fluorine dopant and oxygen vacancies on structural and luminescence characteristics of F doped SnO_2 nanoparticles, Materials 10 (2017), 1398, https://doi.org/10.3390/ma10121398.
[41] G. Cheng, K. Wu, P. Zhao, Y. Cheng, X. He, K. Huang, Solvothermal controlled growth of Zn-doped SnO_2 branched nanorod clusters, J. Cryst. Growth 309 (2007) 53–59, https://doi.org/10.1016/j.jcrysgro.2007.09.007Get.
[42] A. Dieguez, A. Romano-Rodrıguez, A. Vila, J. Morante, The complete Raman spectrum of nanometric SnO_2 particles, J. Appl. Phys. 90 (2001) 1550–1557, https://doi.org/10.1063/1.1385573.
[43] V. Bonu, A. Das, A. Sivadasan, A. Tyagi, S. Dhara, Invoking forbidden modes in SnO_2 nanoparticles using tip enhanced Raman spectroscopy, J. Raman Spectrosc. 46 (2015) 1037–1040, https://doi.org/10.1002/jrs.4747.
[44] M.N. Rumyantseva, A.M. Gaskov, N. Rosman, T. Pagnier, J.R. Morante, Raman surface vibration modes in nanocrystalline SnO_2: correlation with gas sensor performances, Chem. Mater. 17 (2005) 893–901, https://doi.org/10.1021/cm0490470.
[45] Y. Feng, C. Bai, K. Wu, H. Dong, J. Ke, X. Huang, D. Xiong, M. He, Fluorine-doped porous SnO_2@C nanosheets as a high performance anode material for lithium ion batteries, J. Alloys Compd. 843 (2020), 156085, https://doi.org/10.1016/j.jallcom.2020.156085.
[46] Y.-C. Chang, S.-H. Wu, Bi-functional Al-doped ZnO@SnO_2 heteronanowires as efficient substrates for improving photocatalytic and SERS performance, J. Ind. Eng. Chem. 76 (2019) 333–343, https://doi.org/10.1016/j.jiec.2019.03.058.
[47] J.F. Moulder, W.F. Stickle, P.E. Sobol, K.E. Bomben, Handbook of X-Ray Photoelectron Spectroscopy: A Reference Book of Standard Spectra for Identification and Interpretation of XPS Data, Perkin-Elmer Corporation, 1992.
[48] K.S.W. Sing, Reporting physisorption data for gas/solid systems with special reference to the determination of surface area and porosity (recommendations 1984), Pure Appl. Chem. 57 (1985) 603–619, https://doi.org/10.1351/pac198557040603.
[49] J. Hu, C. Zou, Y. Su, M. Li, Z. Yang, M. Ge, Y. Zhang, One-step synthesis of 2D C_3N_4-tin oxide gas sensors for enhanced acetone vapor detection, Sensor. Actuator. B Chem. 253 (2017) 641–651, https://doi.org/10.1016/j.snb.2017.06.176.
[50] V.K. Tomer, S. Duhan, Ordered mesoporous Ag-doped TiO_2/SnO_2 nanocomposite based highly sensitive and selective VOC sensors, J. Mater. Chem. A 4 (2016) 1033–1043, https://doi.org/10.1039/C5TA08336B.
[51] H. Zhao, J. Gao, G. Zhao, J. Fan, Y. Wang, Y. Wang, Fabrication of novel SnO_2-Sb/carbon aerogel electrode for ultrasonic electrochemical oxidation of perfluorooctanoate with high catalytic efficiency, Appl. Catal. B Environ. 136 (2013) 278–286, https://doi.org/10.1016/j.apcatb.2013.02.013.
[52] H. Wang, F. Fu, F. Zhang, H.-E. Wang, S.V. Kershaw, J. Xu, S.-G. Sun, A.L. Rogach, Hydrothermal synthesis of hierarchical SnO_2 microspheres for gas sensing and lithium-ion batteries applications: fluoride-mediated formation of solid and hollow structures, J. Mater. Chem. 22 (2012) 2140–2148, https://doi.org/10.1039/C1JM14839G.
[53] Y. Wang, G. Cheng, Y. Zhang, H. Ke, C. Zhu, Synthesis of fluorinated SnO_2 3D hierarchical structures assembled from nanosheets and their enhanced photocatalytic activity, RSC Adv. 5 (2015) 88079–88086, https://doi.org/10.1039/C5RA15179A.
[54] Y.J. Jeong, W.T. Koo, J.S. Jang, D.H. Kim, M.H. Kim, I.D. Kim, Nanoscale PtO_2 catalysts-loaded SnO_2 multichannel nanofibers toward highly sensitive acetone sensor, ACS Appl. Mater. Interfaces 10 (2018) 2016–2025, https://doi.org/10.1021/acsami.7b16258.
[55] J. Yu, G. Choi, Current–voltage characteristics and selective CO detection of Zn_2SnO_4 and ZnO/Zn_2SnO_4, SnO_2/Zn_2SnO_4 layered-type sensors, Sensor. Actuator. B Chem. 72 (2001) 141–148, https://doi.org/10.1016/S0925-4005(00)00642-0.
[56] Y. Li, H. Ban, M. Yang, Highly sensitive NH_3 gas sensors based on novel polypyrrole-coated SnO_2 nanosheet nanocomposites, Sensor. Actuator. B Chem. 224 (2016) 449–457, https://doi.org/10.1016/j.snb.2015.10.078.
[57] C.-K. Liu, J.-M. Wu, H.C. Shih, Application of plasma modified multi-wall carbon nanotubes to ethanol vapor detection, Sensor. Actuator. B Chem. 150 (2010) 641–648, https://doi.org/10.1016/j.snb.2010.08.026.
[58] D.T.T. Le, N.D. Chinh, B.T.T. Binh, H.S. Hong, N. Van Duy, N.D. Hoa, N. Van Hieu, Facile synthesis of SnO_2–ZnO core–shell nanowires for enhanced ethanol-sensing performance, Curr. Appl. Phys. 13 (2013) 1637–1642, https://doi.org/10.1016/j.cap.2013.06.024.
[59] W. Li, S. Ma, Y. Li, X. Li, C. Wang, X. Yang, L. Cheng, Y. Mao, J. Luo, D. Gengzang, Preparation of Pr-doped SnO_2 hollow nanofibers by electrospinning method and their gas sensing properties, J. Alloys Compd. 605 (2014) 80–88, https://doi.org/10.1016/j.jallcom.2014.03.182.
[60] Y. Guan, D. Wang, X. Zhou, P. Sun, H. Wang, J. Ma, G. Lu, Hydrothermal preparation and gas sensing properties of Zn-doped SnO_2 hierarchical architectures, Sensor. Actuator. B Chem. 191 (2014) 45–52, https://doi.org/10.1016/j.snb.2013.09.002.
[61] Y. Wang, C. Liu, L. Wang, J. Liu, B. Zhang, Y. Gao, P. Sun, Y. Sun, T. Zhang, G. Lu, Horseshoe-shaped SnO_2 with annulus-like mesoporous for ethanol gas sensing application, Sensor. Actuator. B Chem. 240 (2017) 1321–1329, https://doi.org/10.1016/j.snb.2016.07.160.
[62] L. Francioso, C. De Pascali, P. Creti, A.V. Radogna, S. Capone, A. Taurino, M. Epifani, C. Baldacchini, A.R. Bizzarri, P.A. Siciliano, Nanogap sensors decorated with SnO_2 nanoparticles enable low-temperature detection of volatile organic compounds, ACS Appl. Nano Mater. 3 (2020) 3337–3346, https://doi.org/10.1021/acsanm.0c00066.
[63] N. Pienutsa, P. Roongruangsree, V. Seedokbuab, K. Yannawibut, C. Phatoomvijitwong, S. Srinives, SnO_2-graphene composite gas sensor for a room temperature detection of ethanol, Nanotechnology 32 (2020), 115502, https://doi.org/10.1088/1361-6528/abcfea.
[64] D.J. Late, Liquid exfoliation of black phosphorus nanosheets and its application as humidity sensor, Microporous Mesoporous Mater. 225 (2016) 494–503, https://doi.org/10.1016/j.micromeso.2016.01.031.
[65] N.T. Shelke, D.J. Late, Hydrothermal growth of $MoSe_2$ nanoflowers for photo-and humidity sensor applications, Sens. Actuators A Phys. 295 (2019) 160–168, https://doi.org/10.1016/j.sna.2019.05.045.
[66] S.K. Sinha, S. Ghosh, Catalyst-free growth of Al-doped SnO_2 zigzag-nanobelts for low ppm detection of organic vapours, Physica E 84 (2016) 434–443, https://doi.org/10.1016/j.physe.2016.07.019.
[67] C. Agashe, S.S. Major, Effect of heavy doping in SnO_2:F films, J. Mater. Sci. 31 (1996) 2965–2969, https://doi.org/10.1007/BF00356009.
[68] B.J. Wang, S.Y. Ma, S.T. Pei, X.L. Xu, P.F. Cao, J.L. Zhang, R. Zhang, X.H. Xu, T. Han, High specific surface area SnO_2 prepared by calcining Sn-MOFs and their formaldehyde-sensing characteristics, Sensor. Actuator. B Chem. 321 (2020), 128560, https://doi.org/10.1016/j.snb.2020.128560.